Peer-reviewed version available at *Sensors* **2017**, *17*, 2873; doi:10.3390/s17122873

Article

Calibration of binocular vision sensors based on unknown-sized elliptical stripe images

Zhen Liu[1,*], Suining Wu[1], Yang Yin[1] and Jinbo Wu[2,3]

[1] Key Laboratory of Precision Opto-mechatronics Technology, Ministry of Education, Beihang University, No.37 Xueyuan Rd, Haidian District, 100191, Beijing, P. R. China; liuzhen008@buaa.edu.cn; sunnywu1992@buaa.edu.cn; sy1417333@buaa.edu.cn
[2] School of Naval Architecture & Ocean Engineering, Huazhong University of Science & Technology, 1037 Luoyu Road, 430074, Wuhan, Hubei, 430074,P.R.China; hust_wjb@163.com
[3] Hubei Key Laboratory of Naval Architecture & Ocean Engineering Hudrodynamics (HUST) , 430074, Wuhan, Hubei, P. R. China; hust_wjb@163.com
* Correspondence: liuzhen008@buaa.edu.cn; Tel.: +86-10-8233-8768

Abstract: Most of the existing calibration methods for binocular stereo vision sensor (BSVS) depend on high-accuracy target with feature points that are difficult to manufacture and costly. In complex light conditions, optical filters are used for BSVS, but they affect imaging quality. Hence, the use of a high-accuracy target with certain-sized feature points for calibration is not feasible under such complex conditions. To solve these problems, a calibration method based on unknown-sized elliptical stripe images is proposed. With known intrinsic parameters, the proposed method adopts the elliptical stripes located on the parallel planes as a medium to calibrate BSVS online. In comparison with the common calibration methods, the proposed method avoids utilizing high-accuracy target with certain-sized feature points. Therefore, the proposed method is not only easy to implement but is a realistic method for the calibration of BSVS with optical filter. Changing the size of elliptical curves projected on the target solves the difficulty of applying the proposed method in different fields of view and distances. Simulative and physical experiments are conducted to validate the efficiency of the proposed method. When the field of view is approximately 400 mm × 300 mm, the proposed method can reach a calibration accuracy of 0.03 mm, which is comparable with that of Zhang's method.

Keywords: Calibration; Binocular vision sensor; Unknown-sized elliptical stripe

1. Introduction

Calibration of stereo vision sensors is an essential step of vision measurement [1-3]. Vision sensors with high calibration accuracy usually guarantee high measurement accuracy. Vision measurement is mainly conducted to complete the 3D reconstruction of the measured objects. According to the measuring principle, the vision measurement system can be divided into three major categories: (1) line-structured light measurement system; (2) binocular stereo vision measurement system; (3) multi-camera stereo vision measurement system. When adopting the line-structured light method, extraction accuracy of the center of the light stripe affects the measurement accuracy [4-5]. Light scattering occurs when the projection angle between the light plane and the object is relatively large. As a result, calibration and measurement accuracy decline. Multi-camera stereo vision measurement system can implement online vision measurement with large field of view and multi-viewpoints, and it is equivalent to multi-pair binocular stereo vision sensors (BSVSs) [6]. Therefore, research on the calibration of BSVS is of great significance.

To date, research on the calibration of BSVS mainly focused on the different forms of high-accuracy targets, including 1D [7-8], 2D [9], and 3D targets [10-11]. Zhao et al. [12] proposed a method based on a 1D target with two feature points of known distance. Compared with Zhang's method, which is also based on a 1D target, Zhao's method not only improves the calibration accuracy of intrinsic parameters but also implements the extrinsic parameter calibration of BSVS. Zhang's method [14] using the planar checkerboard target has made a remarkable impact on the study of camera calibration. Other methods using rectification error optimization [15] and perpendicularity compensation [16] have been proposed to improve calibration accuracy.

To achieve high-accuracy calibration under complex circumstances, different forms of targets are utilized in the calibration of BSVS. A calibration method based on spot laser and parallel planar target is proposed to improve calibration under complex light conditions [17]. This method does not rely on feature points with known distance or size. In each shot, only one spot is projected on the target, resulting in low efficiency in online measurement. Given that random noise is inevitable, this method cannot guarantee high accuracy due to the location uncertainty of feature points in a picture. Wu et al. [18] proposed a global calibration method based on vanishing features of a target. In addition, the special designed target is constructed of two mutually orthogonal groups of parallel lines with known lengths. Zhang et al. [19] proposed a novel method based on spherical target images with certain size, which implements synchronous calibration of a multi-camera system. At present, the spherical target with extremely high quality is hard to manufacture. Considering the noise, unideal light condition and other factors, using a spherical target to calibrate does not guarantee high accuracy [20-21].

From the abovementioned methods, accuracy of the distance of feature points or the size of the target is a common requirement. In addition, accuracy of the requisite sizes greatly affects the calibration accuracy of BSVS. To solve the problem presented above, this study introduces a novel calibration method that does not rely on specific feature points and works efficiently under complex conditions. The proposed method adapts a ring laser to project an elliptical stripe on the parallel planar target. During the calibration, Zhang's method is primarily utilized to obtain the intrinsic parameter of two cameras. The elliptical stripes are then used as the medium to solve the extrinsic parameters. Finally, the optimal solutions of calibration results are obtained via non-linear optimization.

The remainder of this paper is organized as follows. Section 2 mainly describes the mathematical model of BSVS, the algorithm principles, realization procedure, and other details of the proposed method. Section 3 discusses other expansive forms of the proposed method, as well as its relevant performance in complicated light environment. Sections 4 presents the simulation and real data experiments conducted to validate the effectiveness of the proposed method. Section 5 states the conclusions of our work.

2. Principle and Methods

2.1. Mathematical model of BSVS

As shown in Figure 1, the coordinate systems of the left and right cameras are $O_{c1}x_{c1}y_{c1}z_{c1}$ and $O_{c2}x_{c2}y_{c2}z_{c2}$, respectively. $\tilde{\boldsymbol{p}}_{\mathrm{L}} = [u_{\mathrm{L}} \quad v_{\mathrm{L}} \quad 1]^{\mathrm{T}}$ and $\tilde{\boldsymbol{p}}_{\mathrm{R}} = [u_{\mathrm{R}} \quad v_{\mathrm{R}} \quad 1]^{\mathrm{T}}$ are homogeneous coordinates of non-distorted images of point P in the coordinate system of the image by the left and right cameras, respectively. The transformation matrix from the coordinate system of the left camera to that of the right camera is $\boldsymbol{T}_{\mathrm{LR}} = \begin{bmatrix} \boldsymbol{R}_{\mathrm{LR}} & \boldsymbol{t}_{\mathrm{LR}} \\ 0 & 1 \end{bmatrix}$, where $R_{\mathrm{LR}}, t_{\mathrm{LR}}$ are the rotation matrix and translation vector, respectively. $\boldsymbol{r}_{\mathrm{LR}}$ is the Rodrigues' representation of the rotation matrix R_{LR}.

Peer-reviewed version available at Sensors 2017, 17, 2873; doi:10.3390/s17122873

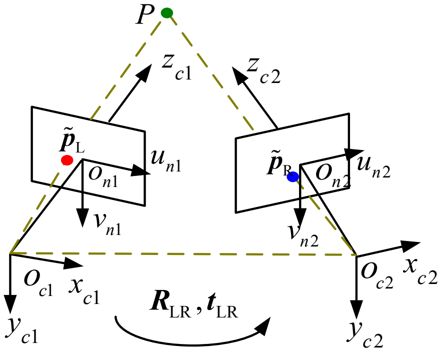

Figure 1. Binocular stereo vision model

The spot P is projected by the BSVS. The binocular stereo vision model is used to calculate the 3D coordinates $\boldsymbol{q}_{\mathrm{L}} = [x_{\mathrm{L}} \quad y_{\mathrm{L}} \quad z_{\mathrm{L}} \quad 1]$ of point P in $O_{c1}x_{c1}y_{c1}z_{c1}$:

$$\begin{cases} \rho_{\mathrm{L}} \tilde{\boldsymbol{p}}_{\mathrm{L}} = \boldsymbol{K}_{\mathrm{L}} [\boldsymbol{I}_{3\times3} \quad \boldsymbol{0}_{3\times1}] \boldsymbol{q}_{\mathrm{L}} \\ \rho_{\mathrm{R}} \tilde{\boldsymbol{p}}_{\mathrm{R}} = \boldsymbol{K}_{\mathrm{R}} [\boldsymbol{R}_{\mathrm{LR}} \quad \boldsymbol{t}_{\mathrm{LR}}] \boldsymbol{q}_{\mathrm{L}} \end{cases} \tag{1}$$

where $\boldsymbol{K}_{\mathrm{L}}$ and $\boldsymbol{K}_{\mathrm{R}}$ are the matrices of intrinsic parameters of the left and right cameras, respectively. $\boldsymbol{K} = \begin{bmatrix} a_{\mathrm{x}} & \gamma & u_0 \\ 0 & a_{\mathrm{y}} & v_0 \\ 0 & 0 & 1 \end{bmatrix}$, where u_0 and v_0 are the coordinates of the principal point, a_{x} and a_{y} are the scale factors in the image u and v axes, and γ is the skew of the two image axes.

2.2. Algorithm principle

The calibration process of the proposed method is shown in Figure 2. In our case, a single ring laser projector and a double parallel planar target are utilized to generate the elliptical stripes as illustrated in Figure 2. In addition, the distance between the two parallel planes is constrained.

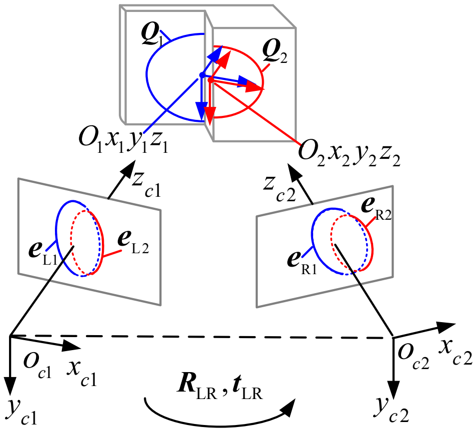

Figure 2. Calibration process of the binocular stereo vision sensor

As shown in Fig. 2, $Q_j\,(j=1,2)$ are the two elliptical stripes projected on the two parallel planes. $Q_j = \begin{bmatrix} 1/\beta_j^2 & 0 & 0 \\ 0 & 1/\alpha_j^2 & 0 \\ 0 & 0 & -1 \end{bmatrix}$ is the expression of the elliptical stripe in space, $2\alpha_j$ is the major axis of the j-th ellipse, and $2\beta_j$ is the minor axis of the j-th ellipse. We assume that $O_j x_j y_j z_j$ is the coordinate of the j-th ellipse in space. For $O_j x_j y_j z_j$, the y-axis is the major axis of Q_j, the x-axis is the minor axis of Q_j, and the origin is the center of Q_j in space. The projections of Q_j in the left and right cameras are denoted as $\boldsymbol{e}_{\mathrm{L}j}$ and $\boldsymbol{e}_{\mathrm{R}j}$, respectively. $\boldsymbol{R}_{\mathrm{L}j}$ and $\boldsymbol{t}_{\mathrm{L}j}$ are the rotation matrix and translation vector from $O_j x_j y_j z_j$ to $O_{\mathrm{c1}} x_{\mathrm{c1}} y_{\mathrm{c1}} z_{\mathrm{c1}}$, respectively. $\boldsymbol{R}_{\mathrm{R}j}$ and $\boldsymbol{t}_{\mathrm{R}j}$ are the rotation matrix and translation vector from $O_j x_j y_j z_j$ to $O_{\mathrm{c2}} x_{\mathrm{c2}} y_{\mathrm{c2}} z_{\mathrm{c2}}$, respectively. $\boldsymbol{R}_{\mathrm{LR}}$ and $\boldsymbol{t}_{\mathrm{LR}}$ are the rotation matrix and translation vector from $O_{\mathrm{c1}} x_{\mathrm{c1}} y_{\mathrm{c1}} z_{\mathrm{c1}}$ to $O_{\mathrm{c2}} x_{\mathrm{c2}} y_{\mathrm{c2}} z_{\mathrm{c2}}$, respectively. All the coordinate frames generated by the intersection of the parallel plane and conical surface projected by the single ring laser projector are parallel to each other, that is, $\boldsymbol{R}_{\mathrm{L1}} = \boldsymbol{R}_{\mathrm{L2}}$ and $\boldsymbol{R}_{\mathrm{R1}} = \boldsymbol{R}_{\mathrm{R2}}$. Notably, the two elliptical stripes captured in each case have the following properties:

(1) The ratios of the minor axis to the major axis $k = \beta_j / \alpha_j$ are equivalent.

(2) The minor axis of the major axis of one elliptical stripe is parallel to that of the other elliptical stripe. The angles between the minor axis and the major axis of these two elliptical stripes are equivalent.

2.2.1. Solving R_{LR}

As shown in Equation (2), $e_{\mathrm{L}j}$ and Q_j are 3×3 matrices. According to multi-view geometry foundation [22], the relationship between $e_{\mathrm{L}j}$ and Q_j is as following:

$$\begin{cases} \boldsymbol{p}^{\mathrm{T}} \boldsymbol{e}_{\mathrm{L}j} \boldsymbol{p} = 0 \\ \boldsymbol{q}^{\mathrm{T}} \boldsymbol{Q}_j \boldsymbol{q} = 0 \end{cases} \tag{2}$$

where $p = [u \quad v \quad 1]^{\mathrm{T}}$ is the undistorted image homogeneous coordinate of the point on the j-th elliptical stripe under $O_{\mathrm{c1}} x_{\mathrm{c1}} y_{\mathrm{c1}} z_{\mathrm{c1}}$, and $q = [x \quad y \quad 1]^{\mathrm{T}}$ is the coordinate of the point on the j-th elliptical stripe under $O_j x_j y_j$.

Combining Equation (2) and the camera model, we have:

$$\rho_j \boldsymbol{Q}_j = (\boldsymbol{K}_{\mathrm{L}} [\boldsymbol{r}_1 \quad \boldsymbol{r}_2 \quad \boldsymbol{t}_{\mathrm{L}j}])^{\mathrm{T}} \boldsymbol{e}_{\mathrm{L}j} \boldsymbol{K}_{\mathrm{L}} [\boldsymbol{r}_1 \quad \boldsymbol{r}_2 \quad \boldsymbol{t}_{\mathrm{L}j}] \tag{3}$$

where ρ_j represents the non-zero scale factors, and r_j denotes the j-th column of the rotation matrix $\boldsymbol{R}_{\mathrm{L}j}$. $\boldsymbol{K}_{\mathrm{L}}$ represents the intrinsic parameter of the left camera and is obtained using Zhang's method.

According to Equation (3), the equation relating $e_{\mathrm{L}j}$ to Q_j is obtained in Equation (4) :

$$\rho_j \boldsymbol{Q}_j = \rho_j \begin{pmatrix} 1/\beta_j^2 & 0 & 0 \\ 0 & 1/\alpha_j^2 & 0 \\ 0 & 0 & -1 \end{pmatrix} = \begin{pmatrix} \boldsymbol{r}_1^{\mathrm{T}} \boldsymbol{W}_j \boldsymbol{r}_1 & \boldsymbol{r}_1^{\mathrm{T}} \boldsymbol{W}_j \boldsymbol{r}_2 & \boldsymbol{r}_1^{\mathrm{T}} \boldsymbol{W}_j \boldsymbol{t}_{\mathrm{L}j} \\ \boldsymbol{r}_2^{\mathrm{T}} \boldsymbol{W}_j \boldsymbol{r}_1 & \boldsymbol{r}_2^{\mathrm{T}} \boldsymbol{W}_j \boldsymbol{r}_2 & \boldsymbol{r}_2^{\mathrm{T}} \boldsymbol{W}_j \boldsymbol{t}_{\mathrm{L}j} \\ \boldsymbol{t}_{\mathrm{L}j}^{\mathrm{T}} \boldsymbol{W}_j \boldsymbol{r}_1 & \boldsymbol{t}_{\mathrm{L}j}^{\mathrm{T}} \boldsymbol{W}_j \boldsymbol{r}_2 & \boldsymbol{t}_{\mathrm{L}j}^{\mathrm{T}} \boldsymbol{W}_j \boldsymbol{t}_{\mathrm{L}j} \end{pmatrix} \tag{4}$$

where $\boldsymbol{W}_j = \boldsymbol{K}_{\mathrm{L}}^{\mathrm{T}} \boldsymbol{e}_{\mathrm{L}j} \boldsymbol{K}_{\mathrm{L}}$.

For two elliptical stripes located on the target, we have two equations in the form of Equation (4). According to the property of the matrix in Equation (4), equations related to the two elliptical stripes can be decomposed into the following 12 equations:

$$\begin{aligned}&\boldsymbol{r}_1^{\mathrm{T}}\boldsymbol{W}_1\boldsymbol{r}_1=\rho_1/\beta_1^2;\boldsymbol{r}_1^{\mathrm{T}}\boldsymbol{W}_2\boldsymbol{r}_1=\rho_2/\beta_2^2;\boldsymbol{r}_2^{\mathrm{T}}\boldsymbol{W}_1\boldsymbol{r}_2=\rho_1/k\beta_1^2;\boldsymbol{r}_2^{\mathrm{T}}\boldsymbol{W}_2\boldsymbol{r}_2=\rho_2/k\beta_2^2;\\&\boldsymbol{r}_1^{\mathrm{T}}\boldsymbol{W}_1\boldsymbol{r}_2=0;\boldsymbol{r}_1^{\mathrm{T}}\boldsymbol{W}_2\boldsymbol{r}_2=0;\boldsymbol{r}_1^{\mathrm{T}}\boldsymbol{W}_1\boldsymbol{t}_{\mathrm{L1}}=0;\boldsymbol{r}_1^{\mathrm{T}}\boldsymbol{W}_2\boldsymbol{t}_{\mathrm{L2}}=0;\\&\boldsymbol{r}_2^{\mathrm{T}}\boldsymbol{W}_1\boldsymbol{t}_{\mathrm{L1}}=0;\boldsymbol{r}_2^{\mathrm{T}}\boldsymbol{W}_2\boldsymbol{t}_{\mathrm{L2}}=0;\boldsymbol{t}_{\mathrm{L1}}^{\mathrm{T}}\boldsymbol{W}_1\boldsymbol{t}_{\mathrm{L1}}=\rho_1;\boldsymbol{t}_{\mathrm{L2}}^{\mathrm{T}}\boldsymbol{W}_2\boldsymbol{t}_{\mathrm{L2}}=\rho_2\end{aligned}\tag{5}$$

Establishing simultaneous equations with the first six equations in Equation (5) and utilizing the orthogonality of $\boldsymbol{r}_1$ and $\boldsymbol{r}_2$, we have:

$$\begin{aligned}&\boldsymbol{r}_1^{\mathrm{T}}\boldsymbol{W}_1\boldsymbol{r}_1=k\boldsymbol{r}_2^{\mathrm{T}}\boldsymbol{W}_1\boldsymbol{r}_2;\boldsymbol{r}_1^{\mathrm{T}}\boldsymbol{W}_2\boldsymbol{r}_1=k\boldsymbol{r}_2^{\mathrm{T}}\boldsymbol{W}_2\boldsymbol{r}_2;\boldsymbol{r}_1^{\mathrm{T}}\boldsymbol{W}_1\boldsymbol{r}_2=0;\boldsymbol{r}_1^{\mathrm{T}}\boldsymbol{W}_2\boldsymbol{r}_2=0;\\&\boldsymbol{r}_2^{\mathrm{T}}\boldsymbol{r}_2=1;\boldsymbol{r}_1^{\mathrm{T}}\boldsymbol{r}_1=1;\boldsymbol{r}_1^{\mathrm{T}}\boldsymbol{r}_2=0\end{aligned}\tag{6}$$

Non-linear optimization is adopted to solve Equation (6). Thereafter, $\boldsymbol{r}_1$ and $\boldsymbol{r}_2$ can be solved directly. According to $\boldsymbol{R}_{\mathrm{L1}}=\boldsymbol{R}_{\mathrm{L2}}=[\boldsymbol{r}_1\quad \boldsymbol{r}_2\quad \boldsymbol{r}_1\times\boldsymbol{r}_2]$, we obtain $\boldsymbol{R}_{\mathrm{L1}}$ and $\boldsymbol{R}_{\mathrm{L2}}$. Similarly, the solution of $\boldsymbol{R}_{\mathrm{R1}}=\boldsymbol{R}_{\mathrm{R2}}$ can be determined.

Taking the target as a medium, the transformation matrix can be obtained as follows:

$$\begin{bmatrix}\boldsymbol{R}_{\mathrm{LR}} & \boldsymbol{t}_{\mathrm{LR}}\\ \boldsymbol{0} & 1\end{bmatrix}=\begin{bmatrix}\boldsymbol{R}_{\mathrm{R1}} & \boldsymbol{t}_{\mathrm{R1}}\\ \boldsymbol{0} & 1\end{bmatrix}\begin{bmatrix}\boldsymbol{R}_{\mathrm{L1}} & \boldsymbol{t}_{\mathrm{L1}}\\ \boldsymbol{0} & 1\end{bmatrix}^{-1}\tag{7}$$

According to Equation (7), we have the final expression of $\boldsymbol{R}_{\mathrm{LR}}$, which is shown in Equation (8) as follows:

$$\boldsymbol{R}_{\mathrm{LR}}=\boldsymbol{R}_{\mathrm{R1}}\boldsymbol{R}_{\mathrm{L1}}^{-1}\tag{8}$$

2.2.2. Solving t_{LR}

Establishing simultaneous equations with the last four equations in Equation (5) yields the following expression:

$$\begin{cases}\boldsymbol{r}_1^{\mathrm{T}}\boldsymbol{W}_1\boldsymbol{t}_{\mathrm{L1}}=0\\ \boldsymbol{r}_2^{\mathrm{T}}\boldsymbol{W}_1\boldsymbol{t}_{\mathrm{L1}}=0\\ \boldsymbol{r}_1^{\mathrm{T}}\boldsymbol{W}_2\boldsymbol{t}_{\mathrm{L2}}=0\\ \boldsymbol{r}_2^{\mathrm{T}}\boldsymbol{W}_2\boldsymbol{t}_{\mathrm{L2}}=0\end{cases}\tag{9}$$

Given that Equation (9) has a typical form of $\mathrm{AX}{=}0$, we cannot obtain a unique non-zero solution $\boldsymbol{t}_{\mathrm{L1}}$ and $\boldsymbol{t}_{\mathrm{L2}}$ by solving Equation (9) directly. Upon analyzing Equation (9), $\boldsymbol{t}_{\mathrm{L1}}$ and $\boldsymbol{t}_{\mathrm{L2}}$ are the center of $\boldsymbol{e}_{\mathrm{L1}}$ and $\boldsymbol{e}_{\mathrm{L2}}$, respectively, which are the coordinates of the origin point of $O_1x_1y_1z_1$ and $O_2x_2y_2z_2$, respectively. Suppose that $\tilde{\boldsymbol{t}}_{\mathrm{L1}}$ and $\tilde{\boldsymbol{t}}_{\mathrm{L2}}$ are the unit vectors from the origin point of $O_{\mathrm{c1}}x_{\mathrm{c1}}y_{\mathrm{c1}}z_{\mathrm{c1}}$ to the origin point of $O_1x_1y_1z_1$ and $O_2x_2y_2z_2$, we have:

$$\begin{cases}\tilde{\boldsymbol{t}}_{\mathrm{L1}}=(\boldsymbol{W}_{\mathrm{L1}}^{\mathrm{T}}\boldsymbol{r}_1\times\boldsymbol{W}_{\mathrm{L1}}^{\mathrm{T}}\boldsymbol{r}_2)/\left\|(\boldsymbol{W}_{\mathrm{L1}}^{\mathrm{T}}\boldsymbol{r}_1\times\boldsymbol{W}_{\mathrm{L1}}^{\mathrm{T}}\boldsymbol{r}_2)\right\|\\ \tilde{\boldsymbol{t}}_{\mathrm{L2}}=(\boldsymbol{W}_{\mathrm{L2}}^{\mathrm{T}}\boldsymbol{r}_1\ /\boldsymbol{W}_{\mathrm{L2}}^{\mathrm{T}}\boldsymbol{r}_2)/\left\|(\boldsymbol{W}_{\mathrm{L2}}^{\mathrm{T}}\boldsymbol{r}_1\ /\boldsymbol{W}_{\mathrm{L2}}^{\mathrm{T}}\boldsymbol{r}_2)\right\|\end{cases}\tag{10}$$

Similarly, the rotation matrix $\boldsymbol{R}_{\mathrm{R1}}=\boldsymbol{R}_{\mathrm{R2}}$ and the translation vectors $\tilde{\boldsymbol{t}}_{\mathrm{R1}},\tilde{\boldsymbol{t}}_{\mathrm{R2}}$ can be solved according to the abovementioned method.

Let $\tilde{\boldsymbol{t}}_{\mathrm{LR}}$ denote the unit vector from the origin point of $O_{\mathrm{c1}}x_{\mathrm{c1}}y_{\mathrm{c1}}z_{\mathrm{c1}}$ to the origin point of $O_{\mathrm{c2}}x_{\mathrm{c2}}y_{\mathrm{c2}}z_{\mathrm{c2}}$. As shown in Figure 3, $\tilde{\boldsymbol{t}}_{\mathrm{L1}}$, $\tilde{\boldsymbol{t}}_{\mathrm{R1}}$ and $\tilde{\boldsymbol{t}}_{\mathrm{LR}}$ lie on a plane.

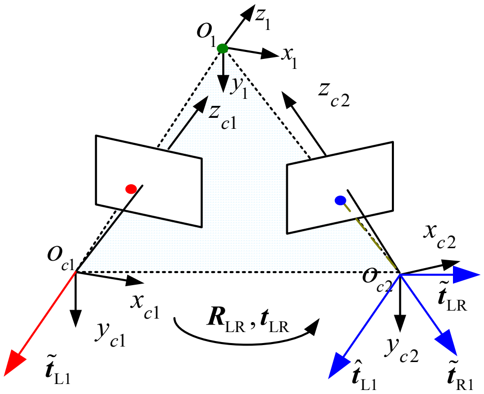

Figure 3. Process to solve $\tilde{t}_{\mathrm{LR}}$

According to the coplanarity constraint, we have:

$$(\hat{\boldsymbol{t}}_{\mathrm{R1}} \times \tilde{\boldsymbol{t}}_{\mathrm{L1}})^{\mathrm{T}} \cdot \tilde{\boldsymbol{t}}_{\mathrm{LR}} = 0 \tag{11}$$

where $\hat{\boldsymbol{t}}_{\mathrm{L1}} = \boldsymbol{R}_{\mathrm{LR}} \tilde{\boldsymbol{t}}_{\mathrm{L1}}$. Suppose that $v = (\hat{\boldsymbol{t}}_{\mathrm{R1}} \times \tilde{\boldsymbol{t}}_{\mathrm{L1}})^{\mathrm{T}}$, the coplanarity constraint can be rewritten as a homogeneous equation in $\tilde{\boldsymbol{t}}_{\mathrm{LR}}$:

$$v \cdot \tilde{\boldsymbol{t}}_{\mathrm{LR}} = 0 \tag{12}$$

If n sets of images of the target are observed, by stacking n such equations as Equation (12), we have:

$$\mathrm{V} \cdot \tilde{\boldsymbol{t}}_{\mathrm{LR}} = 0 \tag{13}$$

where V is an $n \times 3$ matrix. If $n \geq 3$, a unique solution $\tilde{\boldsymbol{t}}_{\mathrm{LR}}$ can be obtained up to a scale factor. Unitizing the solution, we have the unit vector $\tilde{\boldsymbol{t}}_{\mathrm{LR}}$. Given that $\boldsymbol{t}_{\mathrm{LR}} = k_{\mathrm{LR}} \tilde{\boldsymbol{t}}_{\mathrm{LR}}$, Equation (1) can be rewritten as follows:

$$\begin{cases} \tilde{x}_{\mathrm{L}} = \tilde{z}_{\mathrm{L}} u_{\mathrm{L}} / f_{\mathrm{L}} \\ \tilde{y}_{\mathrm{L}} = \tilde{z}_{\mathrm{L}} v_{\mathrm{L}} / f_{\mathrm{L}} \\ \tilde{z}_{\mathrm{L}} = (f_{\mathrm{L}} (f_{\mathrm{R}} \tilde{t}_x - X_{\mathrm{R}} \tilde{t}_z)) / (u_{\mathrm{R}} (r_7 u_{\mathrm{L}} + r_8 v_{\mathrm{L}} + f_{\mathrm{L}} r_9) - f_{\mathrm{R}} (r_1 u_{\mathrm{L}} + r_2 v_{\mathrm{L}} + f_{\mathrm{L}} r_3)) \end{cases} \tag{14}$$

where $\tilde{t}_{\mathrm{LR}} = [\tilde{t}_x, \tilde{t}_y, \tilde{t}_z]^{\mathrm{T}}$.

According to Equation (14), we can obtain the coordinate of a feature point in 3D reconstruction up to a scale factor k_{LR}, that is, $[x_{\mathrm{L}}, y_{\mathrm{L}}, z_{\mathrm{L}}] = k_{\mathrm{LR}} [\tilde{x}_{\mathrm{L}}, \tilde{y}_{\mathrm{L}}, \tilde{z}_{\mathrm{L}}]$. To solve k_{LR}, we reconstruct the 3D coordinates of all the feature points that lie on the ellipse in $O_{\mathrm{c1}} x_{\mathrm{c1}} y_{\mathrm{c1}} z_{\mathrm{c1}}$. Using the plane fitting method, the coefficients of the two plane equations of the target can be determined as follows:

$$\begin{cases} a_{\mathrm{L1}} \tilde{x}_{\mathrm{L1}} + b_{\mathrm{L1}} \tilde{y}_{\mathrm{L1}} + c_{\mathrm{L1}} \tilde{z}_{\mathrm{L1}} + \tilde{d}_{\mathrm{L1}} = 0 \\ a_{\mathrm{L2}} \tilde{x}_{\mathrm{L2}} + b_{\mathrm{L2}} \tilde{y}_{\mathrm{L2}} + c_{\mathrm{L2}} \tilde{z}_{\mathrm{L2}} + \tilde{d}_{\mathrm{L2}} = 0 \end{cases} \tag{15}$$

Where $[a_{\mathrm{L1}}, b_{\mathrm{L1}}, c_{\mathrm{L1}}, \tilde{d}_{\mathrm{L1}}]$ and $[a_{\mathrm{L2}}, b_{\mathrm{L2}}, c_{\mathrm{L2}}, \tilde{d}_{\mathrm{L2}}]$ denote the coefficients of the two plane equations of the target.

Similarly, the plane equations can be determined by fitting the coordinates of all the characteristic points in 3D reconstruction as follows:

$$\begin{cases} a_{\mathrm{L1}} x_{\mathrm{L1}} + b_{\mathrm{L1}} y_{\mathrm{L1}} + c_{\mathrm{L1}} z_{\mathrm{L1}} + d_{\mathrm{L1}} = 0 \\ a_{\mathrm{L2}} x_{\mathrm{L2}} + b_{\mathrm{L2}} y_{\mathrm{L2}} + c_{\mathrm{L2}} z_{\mathrm{L2}} + d_{\mathrm{L2}} = 0 \end{cases} \tag{16}$$

Peer-reviewed version available at *Sensors* **2017**, *17*, 2873; doi:10.3390/s17122873

where $d_{\mathrm{L1}} = k_{\mathrm{LR}}\tilde{d}_{\mathrm{L1}}$, $d_{\mathrm{L2}} = k_{\mathrm{LR}}\tilde{d}_{\mathrm{L2}}$.

According to Equation (14), the distance between the origin of the left camera and the plane, in which the two eclipses lay, can be solved as follows:

$$\begin{cases} Dis1 = \dfrac{\left|a_{\mathrm{L1}}x_{\mathrm{L1}} + b_{\mathrm{L1}}y_{\mathrm{L1}} + c_{\mathrm{L1}}z_{\mathrm{L1}} + d_{\mathrm{L1}}\right|}{\left\|a_{\mathrm{L1}}^2 + b_{\mathrm{L1}}^2 + c_{\mathrm{L1}}^2\right\|} = \left|d_{\mathrm{L1}}\right| \\ Dis2 = \dfrac{\left|a_{\mathrm{L2}}x_{\mathrm{L2}} + b_{\mathrm{L2}}y_{\mathrm{L2}} + c_{\mathrm{L2}}z_{\mathrm{L2}} + d_{\mathrm{L2}}\right|}{\left\|a_{\mathrm{L2}}^2 + b_{\mathrm{L2}}^2 + c_{\mathrm{L2}}^2\right\|} = \left|d_{\mathrm{L2}}\right| \end{cases} \tag{17}$$

Considering that the two planes are parallel and their distance is known, the scale factor k_{LR} is inferred as

$$k_{\mathrm{LR}} = D / \left\| \tilde{d}_{\mathrm{L1}} \right| - \left| \tilde{d}_{\mathrm{L2}} \right\| \tag{18}$$

In this case, the final scale factor k_{LR} is the average of the entire scale factor. Thus, k_{LR} is presented as follows:

$$\boldsymbol{t}_{\mathrm{LR}} = k_{\mathrm{LR}}\tilde{\boldsymbol{t}}_{\mathrm{LR}} \tag{19}$$

2.2.3. Non-linear optimization

Calibration error exists due to random noise and other disturbances. Hence, non-linear optimization is utilized to obtain the optimal solution of calibration results. We randomly sample several feature points from one stripe, and the matching points will be the intersection of the other stripe and corresponding epipolar line.

To improve the calibration accuracy, the target is placed at different positions. For each position, assume that $O_{1\mathrm{i}}x_{1\mathrm{i}}y_{1\mathrm{i}}z_{1\mathrm{i}}$ and $O_{2\mathrm{i}}x_{2\mathrm{i}}y_{2\mathrm{i}}z_{2\mathrm{i}}$ are the target coordinate systems under two parallel planes. For the feature points located on different target planes, we reconstruct their 3D coordinates under the corresponding target coordinate system. Then, the ellipse fitting method is adopted to obtain Q_{1i} and Q_{2i} . From Q_{1i} and Q_{2i} , we can solve the major axes α_{1i} and α_{2i} and minor axes β_{1i} and β_{2i}, as well as the angles θ_{1i} and θ_{2i}. According to the properties of elliptical stripes, the objective function is established as follows:

$$e_1(a) = \min \sum_i^n \left(\left| \frac{\alpha_{1i}}{\beta_{1i}} - \frac{\alpha_{2i}}{\beta_{2i}} \right| + \left| \theta_{1i} - \theta_{2i} \right| \right) \tag{20}$$

where $a = (\boldsymbol{R}_{\mathrm{LR}}, \boldsymbol{t}_{\mathrm{LR}}, \boldsymbol{R}_{\mathrm{Li}}^1, \boldsymbol{t}_{\mathrm{Li}}^1, \boldsymbol{t}_{\mathrm{Li}}^2)$ and $\boldsymbol{R}_{\mathrm{Li}}^1, \boldsymbol{t}_{\mathrm{Li}}^1$ are the rotation matrix and transformation vector, respectively, from the left camera coordinate system to $O_{1\mathrm{i}}x_{1\mathrm{i}}y_{1\mathrm{i}}z_{1\mathrm{i}}$ at each position. $\boldsymbol{t}_{\mathrm{Li}}^2$ is the transformation vector from the left camera coordinate system to $O_{2\mathrm{i}}x_{2\mathrm{i}}y_{2\mathrm{i}}z_{2\mathrm{i}}$, and n denotes the number of positions.

In each position, we reconstruct the 3D coordinates of the feature points under the coordinate system of BSVS. Then, the planar fitting method is utilized to obtain the equation of the left plane Π_{Ai} and right plane Π_{Bi} . Therefore, we obtain the second objective function based on the measurement distance and actual distance:

$$e_2(a) = \min\left(\sum_i^n Dist(\Pi_{Ai}, \Pi_{Bi}) \text{-} D\right) \tag{21}$$

where $Dist(\Pi_A, \Pi_B)$ is the distance of two planes under the coordinate system of BSVS, and D is the actual distance of the two parallel target planes.

According to the coplanarity constraint introduced in section 2.2.2, we have the following objective function:

$$e_3(a) = \min \sum_{i}^{n} ((\boldsymbol{t}_{Ri}^{1} \times \boldsymbol{t}_{Li}^{1})^{\mathrm{T}} \cdot \boldsymbol{t}_{\mathrm{LR}} + (\boldsymbol{t}_{Ri}^{2} \times \boldsymbol{t}_{Li}^{2})^{\mathrm{T}} \cdot \boldsymbol{t}_{\mathrm{LR}}) \qquad (22)$$

where m and l are the feature points in the two target planes, and E is the essential matrix of BSVS.

Thereafter, the final objective function is established as follows:

$$e(a) = e_1(a) + e_2(a) + e_3(a) \qquad (23)$$

Thus, the optimal solution of $\boldsymbol{R}_{\mathrm{LR}}$ and $\boldsymbol{t}_{\mathrm{LR}}$ under the maximum likelihood criteria can be solved via non-linear optimization methods (e.g., Levenberg–Marquardt algorithm [23]).

3. Discussion

The two geometric properties of projected elliptical stripe introduced in section 2.2 comprise the core idea of the proposed method. Notably, various methods are available to obtain the elliptical stripes, such as the use of different forms of lasers or projector to project elliptical stripes on a target plane. Hence, equations in the form of Equation (5) are available to solve the rotation matrix and transformation vector of BSVS. The calibration form used in this study is the simplest form of proposed method. If the axes of the projected light cone in each case remain parallel to each other, the elliptical stripes embody the geometric properties whether the divergence angle of the projective tool is a constant or not. Figure 4 shows several calibration forms for the proposed method.

The lasers shown in Figure 4 are easy to purchase, and the lasers with suitable wavelength and pattern according to the actual condition can be chosen. The BSVS is usually equipped with optical filter, so capturing an ordinary target clearly is difficult. The proposed method adopts the images captured by the strong laser. Thus, this method works much better under complex light conditions such as strong light, dim light, and non-uniform light. In comparison with common methods, the proposed method is more suitable for outdoor online calibration.

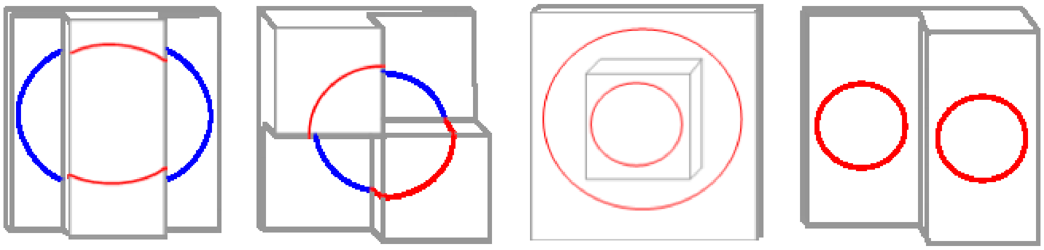
(a) (b) (c) (d)

Figure 4. Combination forms of laser and target. (**a**) Single ring stripe laser and parallel planar target; (**b**) Single ring stripe laser and parallel planar target; (**c**) Concentric double ring stripe laser and parallel planar target; (**d**) Multiple ring stripe laser and parallel planar target.

4. Experiment

4.1. Simulation experiment

Simulation is performed to validate the efficiency of proposed method. Image noise, distance of the two target planes, and size of the projected elliptical stripe considerably affect calibration accuracy when the BSVS is calibrated using the proposed method. Hence, simulation is performed based on the above factors. The conditions of the simulation experiments are as follows: camera resolution of 1628 pixels × 1236 pixels, focal length of 16 mm, field of view is 400 mm × 300mm, placement position is approximately 600 mm away from the BSVS, r_{LR} is [0.0084 0.6822 0.0416], and t_{LR} is [-449.6990 -5.6238 180.8245]$^{\mathrm{T}}$. Calibration accuracy is evaluated using the root mean square errors (RMSEs) of r_x, r_y, r_z, t_x, t_y and t_z, as well as the deviation between the 3D reconstruction and actual coordinates of the feature points.

4.1.1. Impact of image noise on calibration accuracy

In the experiment, the distance between the two target planes is 60 mm. The target is placed at 15 different positions in each experiment, and a total of 100 independent experiments are performed at each noise level. Gaussian noise with zero mean and standard deviation of 0.1-1 pixel with an interval of 0.1 pixel is added to the feature points. As shown in Figure 5, the calibration accuracy decreases linearly with increasing image noise. In general, the calibration accuracy is high even with a relatively high noise level.

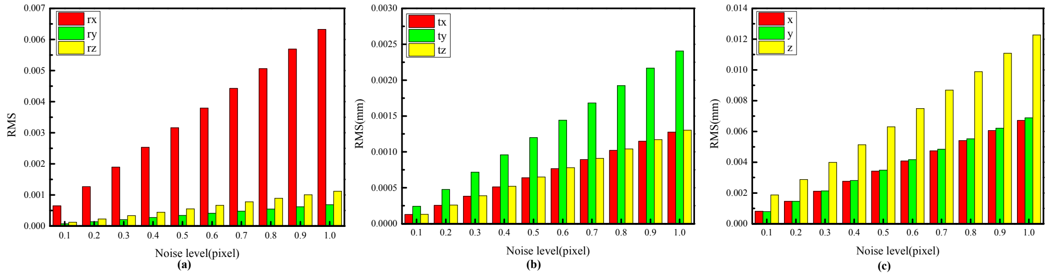

Figure 5. RMSEs of the extrinsic parameters based on the proposed method. (**a**) RMSEs of r_x, r_y and r_z at different noise levels; (**b**) RMSEs of t_x, t_y and t_z at different noise levels; (**c**) RMSEs of the 3D coordinates of the feature points at different noise levels.

4.1.2. Impact of distance between two target planes on calibration accuracy

In the experiment, the distance of two target planes is 60 mm. The target is placed at 15 different positions in each experiment, and a total of 100 independent experiments are performed at each distance level. Gaussian noise with zero mean and standard deviation of 0.5 pixel is added to the feature points. The distance between the two target planes ranges from 10 mm to 100 mm with an interval of 10 mm. As shown in Figure 6a, b, the RMSEs of r_x, t_x, t_y and t_z decrease as the distance levels increase, whereas the RMSEs of r_y and r_z increase as the distance levels increase. As shown in Figure 6c, the calibration accuracy increases remarkably with rising distance level in the range of 10–40 mm but gradually decreases when distance level increases in the range of 40–100 mm. Based on the above analysis, the improvement in calibration accuracy is not entirely related to the increase in distance level. High accuracy can be obtained when the ratio of field of view to the distance between two target planes is 10 (400 mm/40 mm).

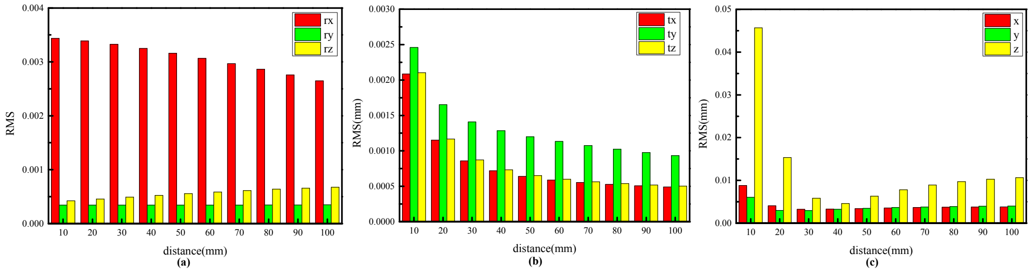

Figure 6. RMSEs of the extrinsic parameters based on the proposed method. (**a**) RMSEs of r_x, r_y and r_z at different distance levels; (**b**) RMSEs of t_x, t_y and t_z at different distance levels; (**c**) RMSEs of the 3D coordinates of the feature points at different distance levels.

4.1.3. Impact of elliptical stripe size on calibration accuracy

In the experiment, the distance between two target planes is 60 mm. The target is placed at 15 different positions in each experiment, and a total of 100 independent experiments are performed at each size level. Gaussian noise with zero mean and standard deviation of 0.5 pixel is added to the feature points. The ratio of the major axes to the minor axes of the elliptical stripe in space is 1.1, and the length of minor axes is from 100 mm to 280 mm with an interval of 20 mm. As shown in Figure

Peer-reviewed version available at *Sensors* **2017**, *17*, 2873; doi:10.3390/s17122873

7a and Figure 7b, the RMSEs of extrinsic parameters decrease as the size levels increase. However, according to the reconstruction errors shown in Figure 7c, the calibration accuracy increases substantially with rising size level in the range of 100–160 mm but gradually decreases when the distance level increases in the range of 160–280 mm. For the proposed method, the most accurate calibration results do not necessarily contribute to the best calibration accuracy. From Figure 7c, the proposed method yields optimal calibration accuracy when the ratio of field of view to the distance between two target planes is approximately 2.5 (400 mm/160 mm).

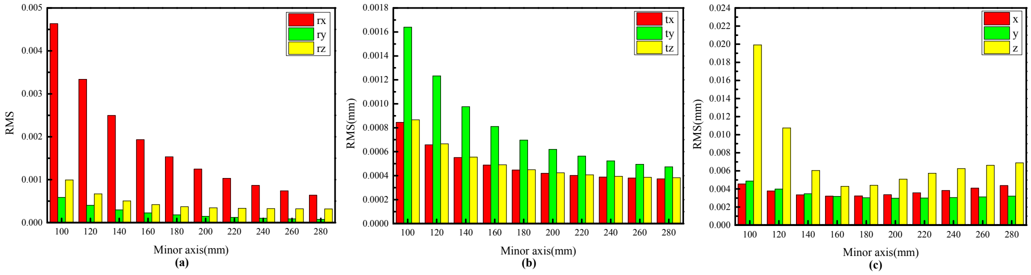

Figure 7. RMSEs of the extrinsic parameters based on the proposed method. (**a**) RMSEs of r_x, r_y and r_z at different distance levels; (**b**) RMSEs of t_x, t_y and t_z at different minor axis length levels; (**c**) RMSEs of the 3D coordinates of the characteristic points at different minor axis length levels.

4.2. Physical experiment

4.2.1. Extrinsic calibration of BSVS

Two sets of physical experiments are performed, namely, the proposed method and Zhang's method. Zhang's method is widely used in camera calibration due to its convenience and efficiency. Hence, we compare the proposed method with Zhang's method.

As shown in Figure 8, two cameras are equipped with the same 16 mm optical lens. The resolution of the camera is 1628 pixels × 1236 pixels, the measurement distance is 600 mm, and the field of view is approximately 400 mm × 300 mm. The resolution of the projector (Dell M110) is 1280 pixels × 800 pixels.

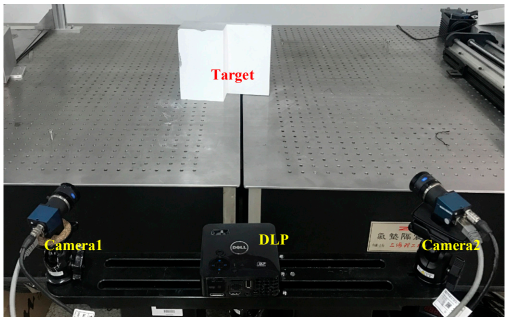

Figure 8. Stereo vision sensor and target.

MATLAB Toolbox in [24] is adopted to complete the intrinsic and extrinsic parameter calibrations of BSVS. A light-emitting planar checkerboard target is used in the physical experiments. The number of feature points on the target is 10 × 10, and the target accuracy is 5 µm. The intrinsic parameter calibration results of two cameras using Zhang's method are shown in Table 1.

Table 1. Intrinsic parameter calibration results of left and right cameras by Zhang's method

	f_x	f_y	u_0(pixel)	v_0(pixel)	γ	k_1(mm^{-2})	k_2(mm^{-4})
Left camera	3672.23	3672.87	833.11	631.99	8.46e-5	-0.11	-0.05
Right camera	3673.59	3672.85	821.11	632.18	-1.59e-5	-0.13	0.92

Peer-reviewed version available at Sensors 2017, 17, 2873; doi:10.3390/s17122873

The calibration process consists of the following steps: (1) the intrinsic and extrinsic parameters of BSVS are calibrated using Zhang's method; (2) the calibration of the proposed method is implemented using the intrinsic parameters calibrated by Zhang's method. The production accuracy of a double parallel planar target is 0.02 mm, and the distance between two target planes is 60.27 mm. The target is placed 15 times in each trial.

The Steger method [25] is adopted to extract the center of the light stripes. Thereafter, the corresponding ellipse is obtained by the ellipse fitting method [26]. Figure 9 shows the results of processing the light stripes in the image. Images used in the two methods are shown in Figure 10.

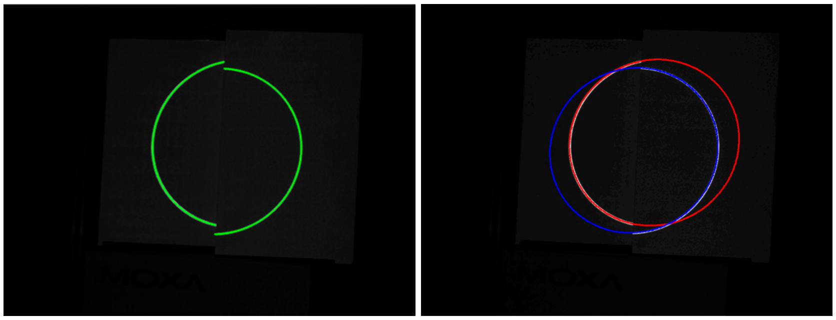
(a) (b)

Figure 9. Result of processing the light stripes in the image. (**a**) Extraction of the center of the light stripes; (**b**) Ellipses obtained by ellipse fitting.

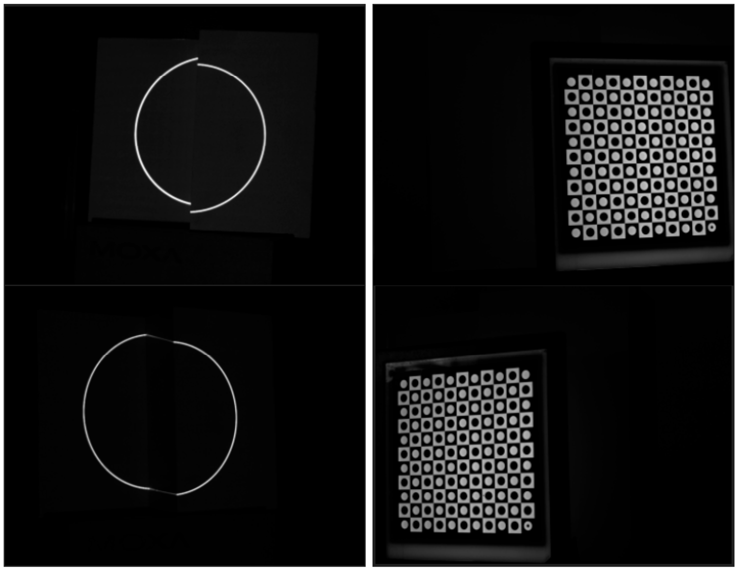
(a) (b)

Figure 10. Images used in calibration via two methods. (**a**) Images used in calibration via the proposed method; (**b**) Images used in calibration via Zhang's method.

Table 2 shows the comparison of the extrinsic parameters calibrated via the two methods. In general, the effects of the two extrinsic calibration methods show no significant difference.

Table 2. Comparison of the extrinsic parameters

	r_x	r_y	r_z	t_x(mm)	t_y(mm)	t_z(mm)
Proposed method	0.0084	0.6822	0.0416	-449.6990	-5.6238	180.8245
Zhang's method	0.0082	0.6845	0.0421	-450.5520	-5.7329	183.8668

4.2.2. Evaluation of the proposed method

To further evaluate the proposed method, the light-emitting planar checkerboard target is placed five times before the BSVS. At each position, the 3D reconstruction coordinates of the feature points on target are computed based on the two methods. Table 3 shows the reconstruction results of five feature points at one of those positions.

Table 3. Comparison of the 3D reconstruction results

Index	Proposed method			Zhang's method		
	x(mm)	*y*(mm)	*z*(mm)	*x*(mm)	*y*(mm)	*z*(mm)
1	100.430	-40.851	578.504	100.550	-40.899	579.197
2	100.732	-30.883	577.749	100.856	-30.921	578.464
3	101.028	-20.922	577.016	101.157	-20.949	577.753
4	91.072	-30.768	575.206	91.185	-30.806	575.923
5	91.676	-10.858	573.712	91.798	-10.872	574.472

The measurement distance d_m of the feature points is computed using the 3D reconstruction coordinates. The actual distance of the feature points on the target coordinate frame is denoted as d_t. The deviation between measurement distance d_m and actual distance d_t is calculated as the reconstruction error Δd. Figure 11a shows the statistical diagram of the data in different reconstruction error levels, and Figure 11b illustrates the box chart showing the statistical analysis of reconstruction error.

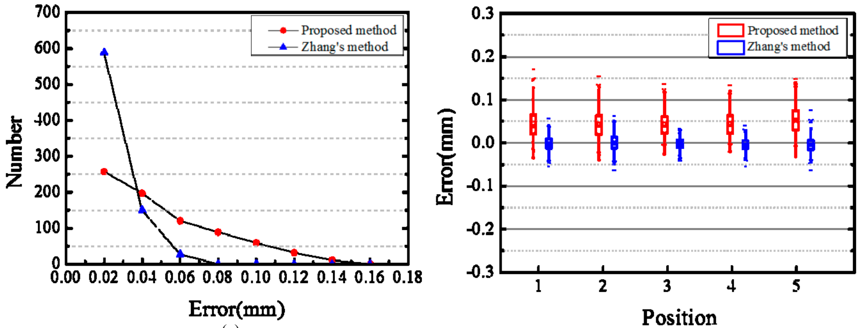

(a) (b)

Figure 11. Reconstruction errors of light-emitting planar target via two methods. (**a**) Number of point pairs in different reconstruction error level via two methods; (**b**) Statistical distributions of the reconstruction error of the feature point pairs via two methods.

From Figure 11a, the distribution of reconstruction errors statistical diagram shows a gradual descending with the increase of error level, where most of the reconstruction errors based on Zhang's method are relatively low. In the box chart, the two short horizontal lines above and below the error bar represent the maximum and minimum values of the data, respectively. As shown in Figure 11b, the deviation between the minimum reconstruction error and zero is relatively large when using the proposed method. The small rectangle in the error bar denotes the mean of the data. Compared with Zhang's method, the mean reconstruction error using the proposed method considerably deviates from zero. The error bar shows the distribution of the data, and its lower and upper boundaries represent 25% and 75% of the data, respectively. Along the direction of the ordinate, the length of the error bar is relatively long in the proposed method than in Zhang's method. For Zhang's method, the reconstruction error is more symmetric about zero, which means that the reconstruction errors are mainly close to zero. The reconstruction RMSEs of the proposed method and Zhang's method are 0.03 and 0.02 mm, respectively. In terms of calibration accuracy, the proposed method is comparable with Zhang's method

Stability is important for the evaluation of a calibration method. Hence, 10 sets of repetitive experiments are performed to validate the efficiency of the proposed method. For each method, 15 sets of images are randomly selected to calibrate the BSVS. Subsequently, repeatability analysis of the calibration parameters and calibration accuracy is conducted. Figure 12 shows the comparison of repeatability analysis of the calibration results.

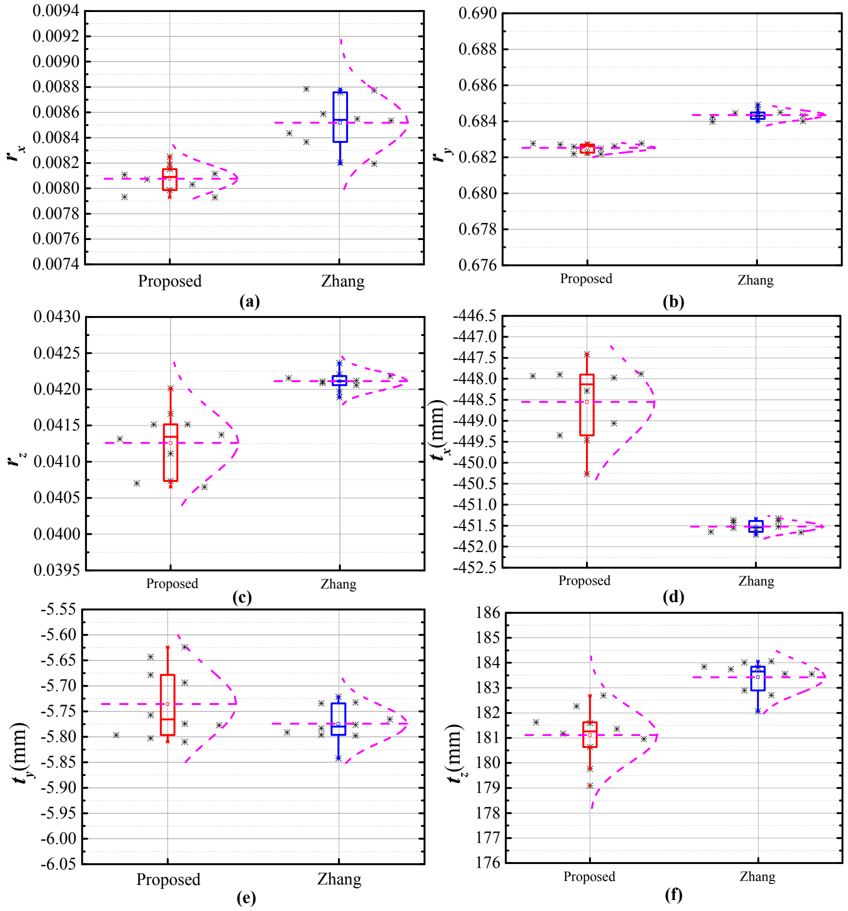

Figure 12. Repeatability of calibration results via two methods. (**a**) Repeatability of r_x via two methods; (**b**) Repeatability of r_y via two methods; (**c**) Repeatability of r_z via two methods; (**d**) Repeatability of t_x via two methods; (**e**) Repeatability of t_y via two methods; (**f**) Repeatability of t_z via two methods.

In Figure 12, the black asterisks represent the calibration parameters, the purple curves are the fitted normal distribution curves of the calibration parameters, and the thin horizontal lines in purple color represent the mean calibration parameters. The shape of the normal distribution curve correlates with the standard deviation of the data. The curve is narrow and high when the standard deviation is low, whereas the curve with a relatively high standard deviation is flat and low. As shown in Figure 12b and Figure 12f, the lengths of error bar of the proposed method is close to that of Zhang's method, meanwhile, the fitted normal distribution curves are similar in shape. Hence, the stability of the proposed method is basically the same as that of Zhang's method. From the Figure 12c, Figure 12d and Figure 12e, the dispersion of the proposed method is high. However, the proposed method performs better in stability as shown in Figure 12a. Accuracy of the calibration method is determined by the entire extrinsic parameter. Hence, the efficiency of the calibration method cannot be evaluated well according to one parameter only. To further prove the stability of the proposed method, we calculated the RMS of the reconstruction errors to present the calibration accuracy of the two methods. Then, the contribution of calibration accuracy is analyzed as shown in Figure 13.

Peer-reviewed version available at Sensors 2017, 17, 2873; doi:10.3390/s17122873

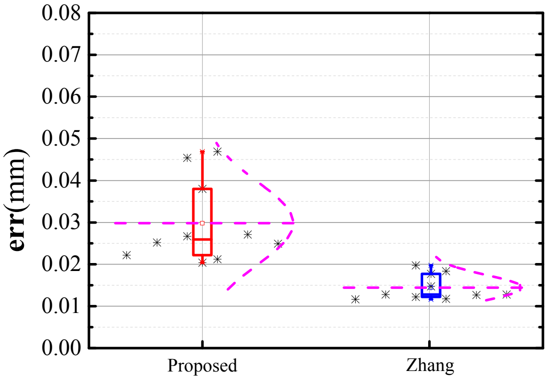

Figure 13. Repeatability of calibration accuracy error via two methods.

In Figure 13, the error bar represents the contribution of calibration accuracy via the two methods. The black asterisks are the entire calibration accuracy data. From the data, the calibration accuracy of Zhang's method is approximately 0.02 mm, and that of the proposed method is close to 0.03 mm. In detail, the majority of calibration accuracy data of the proposed method is less than 0.03 mm. Along the direction of the ordinate, the length of the error bar of the proposed method is approximately twice of that of Zhang's method. Thus, the accuracy data of Zhang's method is relatively concentrated. The thin horizontal lines in purple color represent the mean calibration accuracy. By comparison, the mean calibration accuracy using Zhang's method is close to 0.015mm, which is approximately half of that of the proposed method. In addition, the fitted normal distribution curve of Zhang's method is relatively narrow and high, implying that the calibration accuracy of these methods is highly stable. Based on the above analysis, we have the following evaluation: Zhang's method performs a bit better in stability and calibration accuracy, meanwhile, stability and calibration accuracy of two methods are both relatively high.

The performance of the proposed method is a little bit worse than Zhang's method. However, some methods can be used in the calibration process to further improve calibration accuracy and stability. For instance, we can use multi-planar targets, project multiple elliptical stripes, and adopt enhanced non-linear optimization methods. The proposed method can adopt the feather point, which is not captured by the two cameras simultaneously. In general, the proposed method is slightly inferior to Zhang's method but performs fairly well in practice. Moreover, the proposed method is convenient, flexible, and suitable for dynamic online calibration of BSVS.

5. Conclusions

This paper presents an extrinsic calibration method based on unknown-sized elliptical stripe images. The proposed method avoids using feature points with certain size. Strong light stripes are the core of the proposed method, which is suitable for calibration under complex circumstances. In addition, the proposed method performs well in calibration with an optical filter. The proposed method comes in various forms by flexibly combining the target and elliptical stripe, thereby guaranteeing relatively high calibration accuracy under different conditions. In practice, the planar target can easily ensure high production quality with low cost, and the laser is easily obtained. Several physical experiments validate the efficiency of the proposed method. In conclusion, the proposed method is valuable for practical extrinsic calibration of BSVS.

Acknowledgments: This work is supported by the National Natural Science Foundation of China (NSFC) (51575033, 51679101) and National Key Scientific Instrument and Equipment Development Projects of China (2012YQ140032).

Author Contributions: Zhen Liu, Suining Wu and Yang Yin conceived the article, conducted the experiments, constructed the graphs and wrote the paper. Jinbo Wu helped establish mathematical model.

Conflicts of Interest: The authors declare no conflict of interest.

References

1. Xu, Y. J.; Gao, F.; Ren, H. Y.; Zhang, Z. H.; Jiang, X. Q. An Iterative Distortion Compensation Algorithm for Camera Calibration Based on Phase Target. *Sensors*. **2017,** 17, 1188.
2. LI, Z. X.; Wang, K. Q.; Zuo, W. M.; Meng, D. Y.; Zhang, L. Detail-Preserving and Content-Aware Variational Multi-View Stereo Reconstruction. *IEEE Transaction on Image Processing*. **2016,** 25, 864-877.
3. Poulin-Girard, A. S.; Thibault, S.; Laurendeau, D. Influence of camera calibration conditions on the accuracy of 3D reconstruction. *Opt. Express*. **2016,** 24, 2678-2686.
4. Lilienblum, E.; Al-Hamadi, A. A Structured Light Approach for 3-D Surface Reconstruction With a Stereo Line-Scan System. *IEEE Transactions on Instrumentation & Measurement*. **2015,** 64, 1258-1266.
5. Liu, Z.; Li, X. J; Yin, Y. On-site calibration of line-structured light vision sensor in complex light environments. *Opt. Express*. **2015,** 23, 29896-29911.
6. Seitz, S. M.; Curless, B.; Diebel, J.; Scharstein, D.; Szeliski, R. A Comparison and Evaluation of Multi-View Stereo Reconstruction Algorithms. In Proceedings of the IEEE International Conference on Computer Vision & Pattern Recognition. New York, USA, 17-22 June 2006; pp. 519-528.
7. Wu, F. C.; Hu, Z. Y.; Zhu, H. J. Camera calibration with moving one-dimensional objects. *Pattern Recognit*. **2005,** 38, 755–765.
8. Qi, F.; Li, Q. H.; Luo, Y. P.; Hu, D. C. Camera calibration with one-dimensional objects moving under gravity. *Pattern Recognit*. **2007,** 40, 343-345.
9. Douxchamps, D.; Chihara, K. High-accuracy and robust localization of large control markers for geometric camera calibration. *IEEE Trans. Pattern Anal. Mach. Intell*. **2009,** 31, 376-383.
10. Heikkila, J. Geometric camera calibration using circular control points. *IEEE Trans. Pattern Anal. Mach. Intell*. **2000,** 22, 1066-1077.
11. Tsai, R. Y. A versatile camera calibration technique for high-accuracy 3D machine vision metrology using off-the-shelf TV camera and lenses. *IEEE J. Robot. Autom*. **1987,** 3, 323-344.
12. Zhao, Y.; Li, X. F.; Li, W. M. Binocular vision system calibration based on a one-dimensional target. *Appl. Opt*. **2012,** 51, 3338-3345.
13. Zhang, Z. Y. Camera calibration with one-dimensional objects. *IEEE Trans. Pattern Anal. Mach. Intell*. **2004,** 26, 892-899.
14. Zhang, Z. Y. A flexible new technique for camera calibration. *IEEE Trans. Pattern Anal. Mach. Intell.* **2000,** 22, 1330-1334.
15. Bradley, D.; Heidrich, W. Binocular Camera Calibration Using Rectification Error. *Computer & Robot Vision.* **2000,** 183-190.
16. Jia, Z. Y.; Yang, J. H.; Liu, W. Liu, F. J Y. Wang, Y. Liu, L. L. Wang, C. N. Fan, and K. Zhao, “Improved camera calibration method based on perpendicularity compensation for binocular stereo vision measurement system. *Opt. Express*. **2015,** 23, 15205-15223.
17. Liu, Z.; Yin, Y.; Liu, S. P.; Chen, X. Extrinsic parameter calibration of stereo vision sensors using spot laser projector. *Appl. Opt*. **2016,** 55, 7098-7105.
18. Zhang, H.; Wong, K-Y. K.; Zhang, G. Q. Camera calibration from images of sphere. *IEEE Trans. Pattern Anal. Mach. Intell*. **2007,** 29, 499-503.
19. Wu, X. L.; Wu, S. T.; Xing, Z. H.; Jia, X. A Global Calibration Method for Widely Distributed Cameras Based on Vanishing Features. *Sensors*. **2016,** 16, 838.
20. Ying, X. H.; Zha, H. B. Geometric interpretations of the relation between the image of the absolute conic and sphere images. *IEEE Trans. Pattern Anal. Mach. Intell*. **2006,** 28, 2031-2036.
21. Wong, K-Y. K.; Zhang, G. Q.; Chen, Z. H. A stratified approach for camera calibration using spheres. *IEEE Transaction on Image Processing*. **2011,** 20, 305-316.
22. Hartley, R. I.; Zisserman, A. *Multiple View Geometry in Computer Vision*, 2nd ed.; Cambridge University Press: New York, NY, USA, 2003.
23. J. MORE. The Levenberg-Marquardt Algorithm, Implementation and Theory. *Lecture Notes in Mathematics*. **1978,** 630, 105-116.
24. Bouguet, J.-Y. Camera Calibration Toolbox for Matlab. Available online: http://www.vision.caltech.edu/bouguetj/calib_doc/index.html (accessed on 29 July 2017).
25. Steger, C. An Unbiased Detector of Curvilinear Structures. *IEEE Trans. Pattern Anal. Mach. Intell*. **2002,** 20, 113-125.

26. Fitzgibbon, A.; Pilu, M.; Fisher, R. B. Direct least square fitting of elipses. *IEEE Trans. Pattern Anal. Mach. Intell*. **1999,** 21, 476-480.